^{3,4}He$(\pi^-,n)^{2,3}$H and ^{3}He$(\pi^-,\pi^0)^3$H at 285—575 MeV

L. Orphanos, J. S. McCarthy, and R. C. Minehart
University of Virginia, Charlottesville, Virginia 22901

P. A. M. Gram and B. Höistad*
Los Alamos National Laboratory, Los Alamos, New Mexico 87545

C. F. Perdrisat
College of William and Mary, Williamsburg, Virginia 23185

J. Källne
Smithsonian Astrophysical Observatory, Cambridge, Massachusetts 02138

We have measured the reactions ^{3,4}He$(\pi^-,n)^{2,3}$H at $T_\pi=285$, 428, 525, and 575 MeV over an angular range $\theta_n=18°-134°$ in the center-of-momentum frame, and the reaction ^{3}He$(\pi^-,\pi^0)^3$H at $T_\pi=285$, 428, and 525 MeV over an angular range $\theta_{\pi^0}=60°-140°$. The pion absorption is found to proceed by a two-nucleon mechanism, with an energy dependence consistent with the formation of an $I=\frac{1}{2}$ resonance in the intermediate state. The pion single-charge exchange is discussed within the framework of the optical and Glauber models, and the dependence on the ^{3}He electromagnetic form factors is discussed. We also examine the isospin dependence of the π-nuclear Hamiltonian.

NUCLEAR REACTIONS ^{3,4}He$(\pi^-,n)^{2,3}$H, $T_\pi=285-575$ MeV, $\theta_n=18°-134°$; and ^{3}He$(\pi^-,\pi^0)^3$H, $T_\pi=285-525$ MeV, $\theta_{\pi^0}=60°-140°$; measured $d\sigma/d\Omega$; discussed reaction mechanism, effects of form factors.

I. INTRODUCTION

Pion-induced reactions are fundamental to an understanding of nuclear physics. The pion mediates the long range nuclear force, multiple-pion exchange and pion resonances (e.g., ρ and ω) mediate the short-range forces, and absorption of pions by nucleons gives rise to N^* and Δ resonances, which are believed to be essential ingredients of the nuclear medium. In analogy with quantum electrodynamics (QED), where the fundamental reactions are bremsstrahlung and Compton scattering, the most fundamental pion reactions are absorption, illustrated in Fig. 1, and scattering, illustrated in Fig. 2.

The (π,N) reactions are characterized by large momentum transfers, $q \gtrsim 400$ MeV/c. Because of these high momentum transfers, the cross section would be sensitive to the high-q components (i.e., short range components) of the nuclear wave function if the reaction were to proceed through a single nucleon mechanism. However, a pion cannot be absorbed on a free nucleon, because four-momentum conservation is violated by an amount about equal to the value of the momentum transfer. Consequently, pion absorption (and production) processes require that either the pion or nucleon be driven far off shell. These two conditions, large momentum transfer where $q \sim (1.5-2)k_f$ (k_F=nuclear Fermi momentum) and extreme off-shell behavior (four-momentum nonconservation), are inconsistent with the relatively high cross sections observed, ~ 100 μb/sr, which suggests the possibility of two-nucleon absorption schemes to allow sharing of the momentum transfer.

A particular momentum-sharing mechanism is illustrated in Fig. 3(a). Here the pion is absorbed by a correlated (NN) pair; one of the nucleons is re-
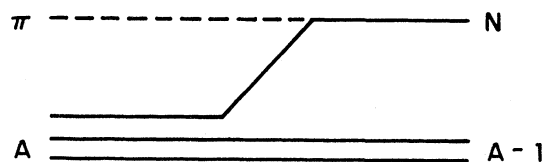

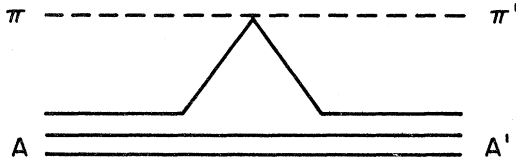FIG. 1. Pion absorption by a single nucleon.
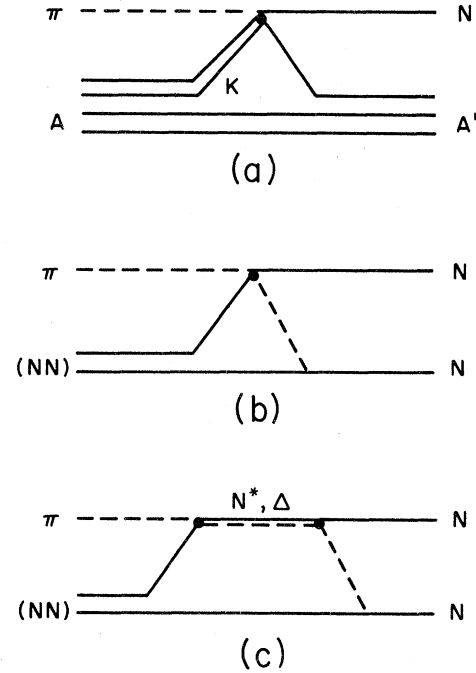
FIG. 2. Pion-nucleon single scattering.

FIG. 3. Pion absorption multinucleon mechanisms; (a) the fundamental two-nucleon mechanism where the pion is absorbed on a correlated (NN) pair; (b) and (c) possible expansions of the upper vertex, rescattering, and intermediate resonances.

moved, and the other rejoins the spectator. One way to describe this reaction is with a factorized representation,

$$\frac{d\sigma}{d\Omega}[A(\pi,N)A-1] \propto \frac{d\sigma}{d\Omega}(\pi d \to pp)F^2(K) \ ,$$

where

$$\frac{d\sigma}{d\Omega}(\pi d \to pp)$$

represents the elementary two-nucleon absorption, with Hamiltonian $H_{\pi NN}$. This vertex contains all the dynamics of the process, and the energy dependence manifests itself here. $F^2(K)$ is a form factor that derives from the probability distribution of a two-nucleon pair in the nucleus A, and contains all the structural (i.e., momentum-transfer) dependence. The two-nucleon vertex can be expanded to contain subprocesses, such as rescattering [Fig. 3(b)] or the excitation of resonances in the intermediate state [Fig. 3(c)].

The (π,π) reaction has two varieties, elastic scattering by π^+ or π^- from protons or neutrons, and pion single-charge exchange (SCE). These reactions proceed through linear combinations of the two isospin channels $I = \frac{1}{2}$ and $\frac{3}{2}$. The interaction may be represented by

$$T = T_s + \vec{I}_\pi \cdot \vec{\tau} T_v \ ,$$

where T_s and T_v are the isoscalar and isovector parts of the T matrix, and where $\vec{I}_\pi$ and $\vec{\tau}$ are the pion and target isospins. Thus, the presumed isospin-rotation invariance of the pion-nuclear Hamiltonian can be examined explicitly by relating pion SCE to elastic scattering.

It has been suggested[1] that pion scattering, through the spin-flip part of the scattering amplitude, would be a sensitive probe of the ^{3}He magnetic form factor at large momentum transfer. This follows because the spin distribution can be expressed as a form factor

$$F_{\text{spin}} \propto (F_m - \tfrac{4}{3}F_c) \ ,$$

where F_m and F_c are the magnetic and charge form factors of ^{3}He. Each of the amplitudes T_s, T_v has a spin-flip dependence $\vec{\sigma} \cdot \hat{n}$, with a momentum depen-

dence determined by $F_{\text{spin}}(q)$.

In this paper we shall discuss the results of experiments[2-4] on pion absorption, ^{3,4}He$(\pi^-,n)^{2,3}$H, and pion SCE, ^{3}He$(\pi^-,\pi^0)^3$H. These data were measured for pion incident energies $T_\pi = 285, 428, 525$, and 575 MeV for (π^-,n), and $T_\pi = 285, 428$, and 525 MeV for (π^-,π^0). The corresponding center-of-mass momentum transfers are $q = 0.4-1.1$ GeV/c for (π,n), where $q = |\vec{p}_\pi - \vec{p}_n|$, and $q = 0.6-1.0$ GeV/c for (π^-,π^0), where $q = |\vec{p}_{\pi^-} - \vec{p}_{\pi^0}|$. These are the highest incident energies and momentum transfers ever measured for these reactions from a complex nuclear system, and extend the kinematic range covered in lower-energy experiments.[5,6]

The helium isotopes offer a particularly good laboratory for such a study: They are in simple angular momentum, spin, and isospin configurations $(l=0, S=0$ or $\frac{1}{2}, I=0$ or $\frac{1}{2})$, and their electromagnetic structures are well known from electron scattering studies.[7,8] Furthermore, the small number of nucleons offers the possibility of microscopic calculations. It also happens that ^{3}He and ^{3}H form the simplest isobaric analog system, whose structures are left relatively intact as they undergo the

transition induced by pion SCE. Finally, the He isotopes lend themselves to a recoil detection technique, where the unique signature of a reaction is the recoil deuteron or triton.

In the sections that follow we discuss in detail the experimental apparatus (Sec. II), the data acquisition and analysis (Sec. III), and the results of the experiments (Sec. IV).

II. EXPERIMENT

For both the $^{3,4}He(\pi^-,n)^{2,3}H$ and the $^3He(\pi^-,\pi^0)^3H$, detection of the appropriate recoiling particle, ^2H or ^3H, provides a unique signature of the reaction. The deuterons and tritons were identified by combinations of measurements of time of flight (TOF), energy loss (ΔE), and the total energy (E). The ^2H or ^3H yield normalized by the incident pion flux was a measure of the relative differential cross sections. Absolute cross sections were extracted by comparison with other experiments.

A. Pion beam

This experiment was performed in the high-energy pion[9] channel of the Clinton P. Anderson Meson Physics Facility (LAMPF). A pion flux of nominally 10^7 sec^{-1} was obtainable, within a momentum bite $\Delta p/p=0.05$ and with 6% duty factor. The spot size was 1.5 cm horizontal ×2.5 cm vertical FWHM. The beam profile and momentum were fine-tuned with a current-integrating xy wire chamber[10] temporarily placed in the beam at the target location.

The beam flux was monitored with an ionization chamber, consisting of three plates of Al foil held at a potential difference of 300 V, immersed in a continuously flushed Ar-CO_2 gas mixture. Muon and electron contamination of the beam was small,[9] ∼1%.

A second monitor[11] was a scintillator telescope that detected the forward-directed muon halo from the in-flight decay of the pions. These decay muons were used for:

(1) a stability check for the beam—the ratio

$$\frac{\pi_\mu - \pi_\mu \text{ accidentals}}{\text{ion chamber}}$$

should be a constant for all runs of a given energy, where π_μ denotes the number of $\pi \rightarrow \mu + \nu$ events

detected.

(2) a determination of computer dead time. This was done by scaling both computer-gated and nongated π_μ counts. Then

$$\frac{(\pi_\mu - \pi_\mu \text{ accidentals})_{\text{gate}}}{(\pi_\mu - \pi_\mu \text{ accidentals})_{\text{no gate}}} = \frac{\text{live time}}{\text{total time}}$$

$$= 1 - \frac{\text{dead time}}{\text{total time}} .$$

The ion-chamber counts were reduced appropriately to correct for the pion flux that was measured while the computer was unable to process the corresponding events.

Three methods were used to obtain an absolute normalization, which were found to agree within 10%:

(1) comparison of the 285 MeV (π^-,n) spectra to overlapping spectra of a previous experiment.[5]

(2) comparison of the πp elastic scattering to published values.[12,13] This was done by measuring the yield of monoenergetic protons from elastic scattering in a CH_2 target (with appropriate subtraction of the ^{12}C background), and comparing the resulting differential cross section to those previously measured.

(3) placement of the detector of 0°, reducing beam intensity, and counting the number of pions directly as a function of ion chamber counts.

B. Target system

The target system was a cryostat which could maintain liquid ^3He and superfluid ^4He in separate target cells. The SD-100 cryostat, operated by the University of Virginia, has been described elsewhere[7]; its configuration is represented schematically in Fig. 4. The Dewar was 0.6 m in diameter and approximately 2 m in height. The outer vacuum shield was made of aluminum, and had two halves that were bolted together with an O-ring seal. The top half had the liquid N_2 and ^4He baths and target cell assembly welded inside; the bottom half was a container with two windows of 0.0094 cm 5056 H18 aluminum diametrically situated to admit pions and allow reaction particles to escape. The bottom half also contained two heat shields (aluminized Mylar with 0.0076 cm thick Al windows) to suppress radiative heating of the target cells.

The N_2 bath held 25 l and was in thermal contact with the outermost heat shield. The ^4He (4.2 K)
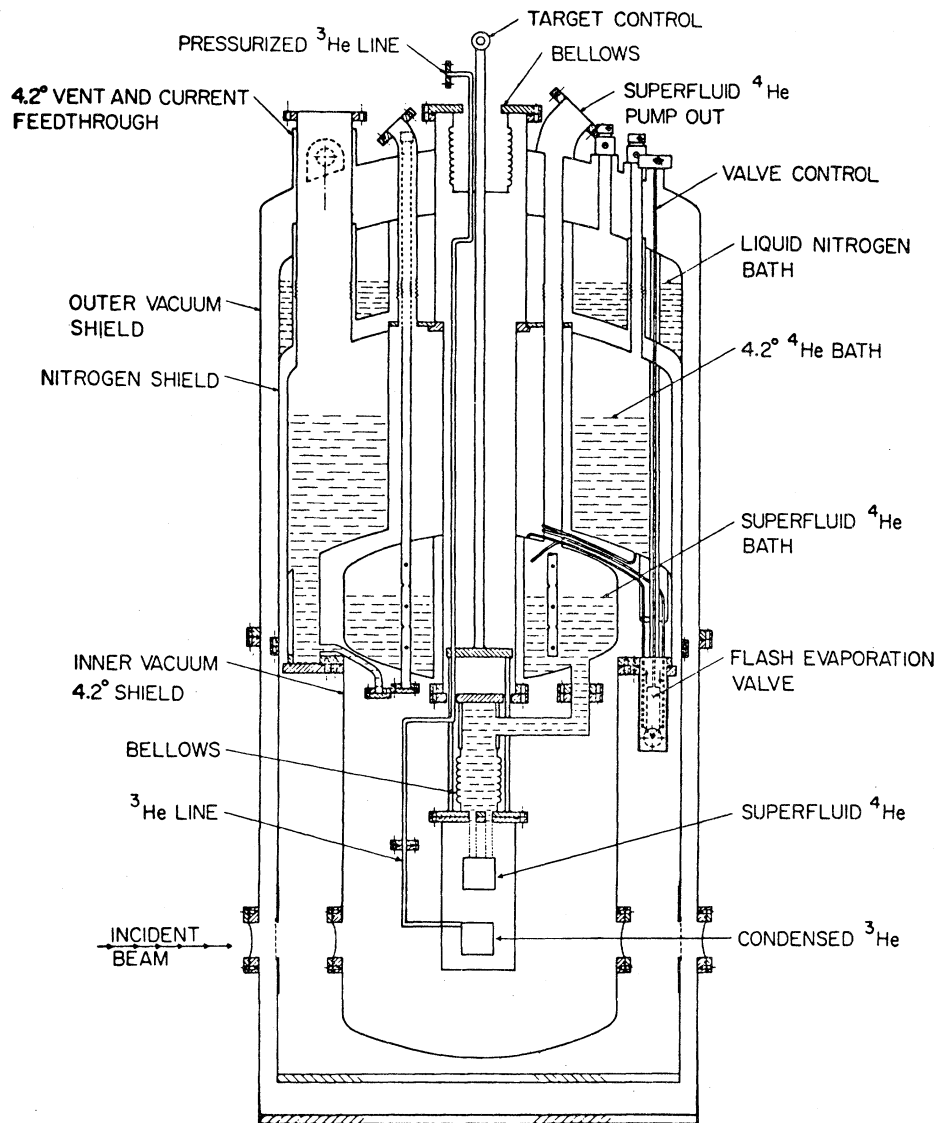
FIG. 4. Cross section of target apparatus.

bath held 50 l and was in thermal contact with the innermost heat shield. The 4.2° bath was connected to the super-fluid ^{4}He bath (1.5 K) via a stainless-steel tube and flash evaporation valve; the 1.5° bath held 15 l and was in thermal contact with the target cells.

The target cells were 12.5 cm square, and were two separate empty spaces in a 1.5 cm Cu block. The cells had windows of the same Al foil as the outer vacuum windows; the Al window/Cu block interface was joined with an indium seal. The superfluid ^{4}He was fed into the uppermost cell from the 1.5° bath via tubes through the bellows mechanism; gaseous ^{3}He was condensed into and recovered from the lower cell via an isolated line from an

external ballast tank. The bellows allowed raising or lowering the target cells to position them in the beam. The ^{3}He cell could be filled and evacuated without affecting internal operating parameters significantly; thus we had an empty cell to use for background measurements.

While in operation, the Dewar had boil-off rates of $\sim\frac{1}{2}$ l/h for the $N_{2(l)}$ and $^4He_{(l)}$ at atmospheric pressure, and $\sim\frac{1}{5}$ l/h for the pumped-on superfluid ^{4}He at a pressure ~ 30 mm Hg. In practice, the $N_{2(l)}$ and ^{4}He (4.2°) baths were refilled once a day, and the ^{4}He (1.5°) bath was refilled every two days. The level of the fluid in each bath was monitored by resistive level indicators, and internal temperatures at various points inside the Dewar were moni-

tored with Speer grade 1002 resistors. The temperature of the superfluid ^{4}He was monitored with a precision pressure gauge on the 1.5° bath pump port.

Relevant target parameters are summarized in Table I. The aluminum ($\rho=2.7$ g/cm^3) presented material as in Table II, where the contribution from air at 10^{-6} Torr is negligible. The aluminium in the beam was the primary source of background, but this was minimized by a choice of detector angles so that the detector saw the target approximately face-on. Effective background densities are shown in Table III. As can be seen by comparing relative densities (Table IV), this was a more serious problem for ^{3}He than for ^{4}He.

C. Detector

The detector was required to identify deuterons and tritons among the plethora of pions, nucleons, deuterons, tritons, and helium ions that were produced. This was done by measuring kinetic energy (E), energy loss (ΔE), and time of flight (TOF) for each event that triggered the detector.

Consider a nonrelativistic particle of velocity β ($c=1$). If $\beta=d/\text{TOF}$, where d is a distance fixed by the geometry of the detector, then $E=\frac{1}{2}m$ $(d/\text{TOF})^2$, and

$$m=\frac{2}{d^2}E\cdot(\text{TOF})^2 \ .$$

Thus, a measurement of E and TOF uniquely determines m. For a relativistic particle, $\beta=d/\text{TOF}$ and

$$E=\frac{m}{(1-\beta^2)^{1/2}}-m \ ,$$

which gives

$$e=\frac{E[(\text{TOF})^2-d^2]^{1/2}}{\text{TOF}-[(\text{TOF})^2-d^2]^{1/2}} \quad (c=1) \ .$$

TABLE I. Target parameters.

Target	Target density (gm/cm^3)	Target thickness (cm)	Target angle	Effective density[a] (gm/cm^2)
^{3}He	0.080	0.635	45°	0.0718
^{4}He (4 K)	0.128	0.635	45°	0.1145
^{4}He (1.9 K)	0.1454	0.635	45°	0.1301

[a]Effective density = density × thickness/cos(angle).

TABLE II. Background material (aluminum).

Cell window (cm)	Heat shields (cm)	Vacuum window (cm)	Total (cm)
0.0094	0.0008	0.0094	0.0196

Similarly, the well-known Bethe-Bloch[14] equation for energy loss gives

$$\frac{dE}{dx}\propto\frac{Z^2}{m\beta^2} \ .$$

The factor $m\beta^2$ is proportional to the nonrelativistic kinetic energy, and to the relativistic kinetic energy to first order. Then

$$m=\frac{Z^2}{\left[\dfrac{dE}{dx}\right]\beta^2} \ ,$$

which in the limit

$$\frac{dE}{dx}=\frac{\Delta E}{\Delta x}$$

(true for scintillators with small thickness Δx) can be written

$$m=\frac{Z^2\Delta x}{\Delta E\times\dfrac{2E}{m}} \ .$$

Thus,

$$m=\left[\frac{Z^2\Delta x}{2E\cdot\Delta E}\right]^{1/2} \ ,$$

a unique function of E and ΔE. In practice, particles of $Z\geq2$ were excluded because their large energy loss did not permit them to penetrate the detector sufficiently to generate a trigger.

The detector consisted of five plastic scintillators (Pilot B) and two multiwire proportional counters (MWPC). The light from scintillators $S1$, $S2$, and

TABLE III. Background densities.

Traversing particles	Thickness of Al (cm)	Relative angle	Effective background[a] density (g/cm^2)
beam	0.0196	45°	0.078
reaction products	0.0196	0°	0.053

[a]Effective background density $=\rho_{\text{Al}}\times$ thickness/cos(angle) and $\rho_{\text{Al}}=2.7$ g/cm^2.

TABLE IV. Target: Background density ratios.

Target material	Effective target density (g/cm^2)	Effective background density presented to beam (gm/cm^2)	Target background
^{3}He	0.0718	0.078	0.921
^{4}He (4 K)	0.1145	0.078	1.468
^{4}He (1.9 K)	0.1301	0.078	1.668

TABLE V. Geometrical parameters of the detector.

Device	Height (cm)	Width (cm)	Thickness (cm)	Distance from target[a] (cm)
S1	12.70	30.48	0.1588	38.10
MWPC1[b]	15.24	48.26		45.09
MWPC2[b]	15.24	48.26		66.04
S2	12.70	48.26	0.3175	71.86
S3	15.24	48.26	0.3175	88.27
S4	15.24	50.80	15.24	92.08
S5	20.32	55.88	0.635	111.76

[a]Target center=3 m focus of pion beam.
[b]Height and width of active area.

$S3$ gave three different measurements of ΔE, and the summed light from $S1$, $S2$, $S3$, and $S4$ was a measure of total energy E. The difference in arrival time of signals from $S1$, $S2$, and $S3$ gave two independent values of TOF. $S5$ was a veto counter, and was part of the trigger logic only. The MWPC's determined the coordinates (x_1,y_1) and (x_2,y_2) for each event, which gave trajectory and angular information. The detector is represented schematically in Fig. 5, and a geometrical summary is given in Table V. It is seen in Fig. 5 that the elements of the detector do not have their geometric centers in line. This was an intentional part of the design, done in order to maximize the accessible angular range.

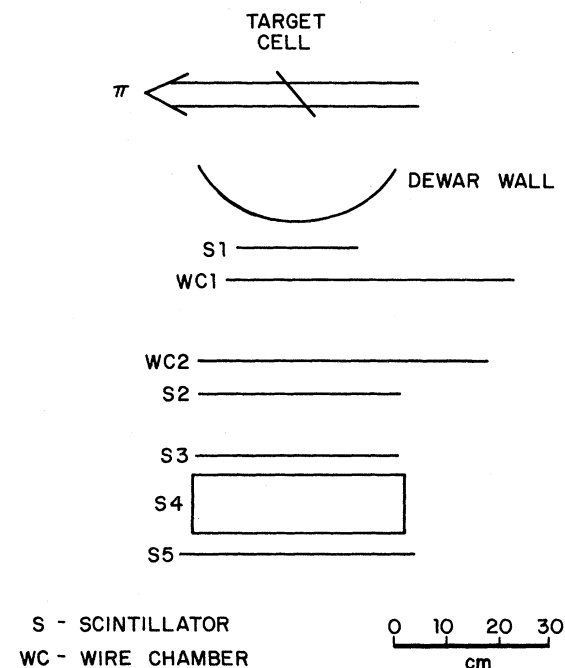$S1-S3$ and the MWPC's were mounted by support brackets to one side of a movable cart. The support brackets were movable along fixed rails on the side of the cart, so that TOF and trajectory-measuring distances could be adjusted as desired. $S4$ and $S5$ were placed on a table behind $S3$. The detector cart had an angular range $\theta=32.5°-142.5°$ about its center of rotation.

$S1-S3$ were mated to adiabatic, isochronous light guides along their long edges (top and bottom); these light guides were coupled to EMI 9813 (5.1 cm diameter, 14 stage) photomultiplier tubes. $S5$ had a similar light guide and phototube along one 20.3 cm edge, and $S4$ had a light guide and 12.7 cm diameter 14-stage phototube on one 15×15 cm^2 end.

Gathering light from both sides of $S1$, $S2$, and $S3$, rather than just one side, has several advantages:

(1) elimination of position dependence from TOF measurements,

(2) minimization of the attenuation and dispersion of light pulses, and

(3) decrease of light lost due to imperfect reflection, thus suppressing the "under measurement" of ΔE.

Two light guides and phototubes on $S4$ would have provided the same advantages, but physical constraints imposed by the need for angular range prevented it. $S5$ was used only for its logic signal, so the analog signal quality was of less concern.

The MWPC's were external delay line wire chambers (2.5 nsec/cm), which were capable of high count rates (10^5-10^6 sec^{-1}). These chambers consisted of two plastic frames; one frame had tightly-stretched wires of Au-plated W in one direction, equally spaced at 4 mm, and the other frame had wires of Au-plated Cu-clad Al at 1 mm spacing.

FIG. 5. Schematic diagram of detector apparatus.

These planes were anode and cathode, respectively, and were kept at a potential difference of 2300 V. The wire planes were mounted in an Al case, with a 0.0025 cm Mylar foil and a 0.005 cm Al foil for each of the entrance and exit windows. The chambers were continually flushed with a mixture of 75.8% Ar, 20% isobutane, 4% methol, and 0.2% freon (% by volume). Relevant density parameters of the detector are tabulated in Table VI.

Particles that did not have sufficient range to reach $S2$, or that had so large a range that they were not stopped by $S4$, did not satisfy the logical

constraints of the trigger. The limitations imposed on a reaction particle that was required to have a stopping distance somewhere between $S2$ and $S4$ necessarily limit the dynamic range of the detector, which is listed in Table VII.

The MWPC's were capable of resolving single anode wires, equivalent to 4 mm position resolution. Since the first MWPC was 450 mm from the target, this gave an angular resolution

$$\tan^{-1}(\tfrac{4}{450})=0.5° .$$

The angular acceptance of the detector was

$$2\tan^{-1}\left|\frac{\text{half-width of }S4}{\text{focus-}S4\text{ distance}}\right|=2\tan^{-1}\left|\frac{254\text{ mm}}{920.75\text{ mm}}\right|=30.8° ,$$

while the maximum solid angle possible was

$$\Delta\Omega=\frac{S4\text{ area}}{(\text{focus-}S4\text{ distance})^2}=\frac{(482.6\text{ mm}\times127\text{ mm})}{(920.75\text{ mm})^2}=72.3\text{ msr} ,$$

where $S4$ dimensions have been decreased 26.5 mm on a side to exclude "edge effects." A more conservative solid angle was defined by accepting events whose trajectories intersected the central region of the second MWPC;

$$\Delta\Omega=\frac{(308.1\text{ mm}\times109\text{ mm})}{(660\text{ mm})^2}=71.4\text{ msr} .$$

There was a 6% uncertainty to the acceptance because of the finite size of the beam spot on the target (cf. Table IX).

D. Data acquisition and reduction

The large solid angle and energy bite of our detector resulted in the measurement of many background events. Primary sources of these were minimum-ionizing particles, and protons, deuterons, and tritons that had been knocked out into

the continuum by pion collision with target walls, etc. These undesirable events were suppressed in part by appropriate choice of the event trigger.

The triggers used were the following:

$$T_1=S1_H\cdot S2_L\cdot\overline{MI}, \quad T_2=S1_L\cdot S2_L\cdot S3_L\cdot\overline{MI} ,$$

$$T_3=S1_H\cdot S2_L\cdot S3_L\cdot\overline{MI}, \quad T_4=S1_L\cdot S2_L\cdot S3_L ,$$

where

$$MI=(S1_L\cdot S2_L\cdot S3_L\cdot S5)$$

$$=\text{minimum-ionizing event} .$$

In each case, $S_i=S_iA+S_iB$, where A and B refer to the top and bottom phototube, respectively, of the ith scintillator. H and L refer to high or low discriminator thresholds: $L=300$ mV, approximately the pulse height for minimum-ionizing particles, and H was varied between 450−900 mV, as the situation required.

T_1 was used to suppress high-energy particles,

TABLE VI. Density parameters of the detector. All entries in g/cm^2. $\rho_{air}=0.00129$, $\rho=2.7$, and $\rho_{scintillator}=1.02$.

Device	Dewar	S1	MWPC	S2	S3	S4
preceding/ enclosed air	0.0	0.010	0.036	0.007	0.021	0.005
Al-Mylar	0.053	0.015	0.065	0.016	0.016	0.016
scintillators	0.0	0.162	0.0	0.324	0.324	15.54 (to back)
total		0.053	0.187	0.101	0.347	0.361	15.56

TABLE VII. Dynamic range of the detector.

Particle	Minimum range (to $S2$)	Maximum range (through $S4$)	E_{min} (MeV)	E_{max} (MeV)
p			18	155
	0.34 g/cm^2	16.61 g/cm^2		
d			25	210
t			30	250

when desired reaction particles would stop in $S2$ or $S3$. T_2 suppressed low-energy events; it insisted that particles have sufficient energy to penetrate $S4$. T_3 was a "tight" trigger for particles that would stop in $S3$, or just barely penetrate and stop in $S4$. T_4 was used only for detector calibration runs, when minimum-ionizing particles were desirable.

The trigger pulses were 200 nsec long; the pulse length was defined by the requirement that all scintillator and MWPC signals from an event have time to activate the electronics. The trigger was used as a "start" pulse for the TDC's and as a "gate" pulse for the ADC's. Analog signals from the scintillators gave a measure of energy deposition. The arrival-time differences with respect to the leading edge of the trigger pulse were translated into TOF. Similarly, the arrival-time differences of MWPC signals were translated into (xy) coordinates. The electronics were of standard NIM and CAMAC (Ref. 15) configuration, and are illustrated along with the trigger logic in Fig. 6. The data were recorded on

FIG. 6. Trigger logic and data acquisition.

magnetic tape by a PDP 11/34 computer for subsequent off-line analysis.

In the analysis, one must first sort "good" events from "bad" ones. A good event is defined as one whose trajectory both originates from the target and also falls within a prescribed solid angle that excludes the possibility of multiple scattering out of the sides of scintillator $S4$. A bad event is one that generated a trigger in the logic despite a misfire in the wire chambers (so that trajectory information is not available), or one that had an unphysical trajectory (indicating that the trigger was really a random coincidence). For the good events, one computes a TOF, various energy losses ΔE (in the scintillators, $S1$, $S2$, and $S3$), and their total energy E, from which are constructed scatter plots ΔE vs E and TOF vs E. This results in clear separation of the events along lines of constant mass. The mass appropriate to the reaction under consideration is chosen; for example, with a ^{3}He target one chooses the triton band for (π^-, π^0), or the deuteron band for (π^-, n). These events are then plotted as a function of energy. From the resulting histogram one can identify the peak at the energy corresponding to the appropriate two-body reaction, and the differential cross section can be extracted. These steps are described in detail below.

The event-by-event processing proceeded as follows:

(1) A sum-time calculation was performed for each plane (x and y) of each MWPC.[2] This involved taking the *sum* of the time signals from opposite sides of the plane; the result should be

$$t_1 + t_2 = \frac{d}{u} = \frac{\text{length of chamber active dimension}}{\text{propagation speed of pulse}},$$

a constant of the chamber plane independent of position. If the summed times did not fall within prescribed limits, the chamber was deemed to have misfired. Reliable trajectory information could not be calculated if two or more planes misfired, and the event was rejected. Efficiencies were computed for each plane by counting the fraction of events where that plane had a bad sum time and the other three planes had good ones. That fraction was then the probability that the plane would misfire. Appropriate combination of these probabilities yielded the compound probability that two or more planes misfired, thus resulting in a good event being rejected. A correction for this inefficiency was included in the computation of the differential cross sections. Details are given in Ref. 2.

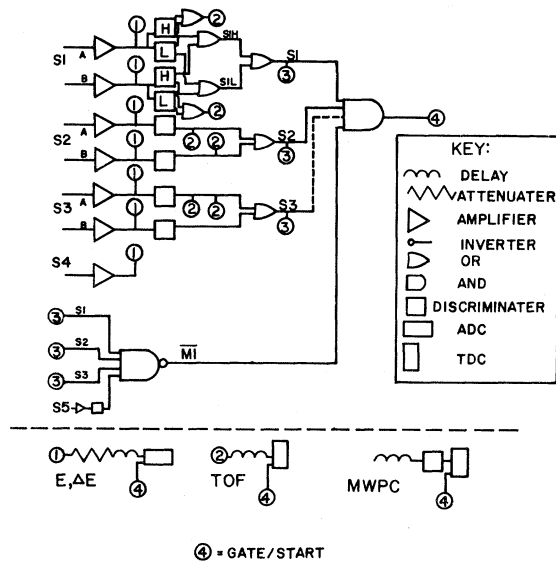(2) For events with good sum times, the trajectory

was computed. Events with trajectories that did not fall within solid angle limits designed to exclude the possibility of multiple scattering out the sides of the detector, and events with trajectories not originating from the target cell, were rejected.

(3) The times of flight $T_{21}=S2-S1$ and $T_{31}=S3-S1$ were calculated. These TOF's are not rigorously correct, because the detected particle lost energy traversing the preceding material, but these energy losses were negligible in their effect on the mass identifications.

(4) For each of the scintillators $S1$, $S2$, and $S3$ there were two photomultiplier tube signals, A and B (one from each end). The net analog signal was defined as the geometric average,

$$S_i(S_{iA} \cdot S_{iB})^{1/2},$$

to minimize position-dependent response effects. $S4$ required an explicit position response correction, because it was rather long (50.8 cm) and had a tube at only one end. The measured light pulse amplitude was multiplied by a factor $f(x)=0.0047x + 1.0333$, where x is the position of the event, measured in cm from the center of $S4$ (-25.4 cm $<x<25.4$ cm; phototube at -25.4). This response function was determined by measuring the light output from $S4$, using a radioactive source placed at fixed positions.

Light output is related to energy loss[16] (to first order) by

$$\frac{dL}{dx}=\frac{A\left|\dfrac{dE}{dx}\right|}{1+B\left|\dfrac{dE}{dx}\right|},$$

where dL/dx is the differential light production, dE/dx is the differential energy loss, and A and B are constants that depend on the nature of the material. Setting

$$\frac{dE}{dx}=\frac{C}{E},$$

one has

$$\frac{dL}{dx}=\frac{AC}{E+BC}$$

where C is mass dependent. For these thin scintillators,

$$\frac{dL}{dx}=\frac{L}{\Delta x/\cos\theta},$$

where $\Delta x=$scintillator thickness and θ is the scattering angle of the detected particle; it is

straightforward to determine E from L. We define $\Delta E_1=$energy output from $S1$, $\Delta E_2=$energy from $S1+S2$, $\Delta E_3=S1+S2+S3$, and $E=\Delta E_3+S4$.

From the TOF, ΔE, and E the masses can be directly identified. Some typical scatter plots of ΔE vs E and TOF vs E are shown in Fig. 7. Note the well-separated mass bands; in general, resolution of the mass identifications was excellent. Reading from the bottom upwards on each scatter plot of
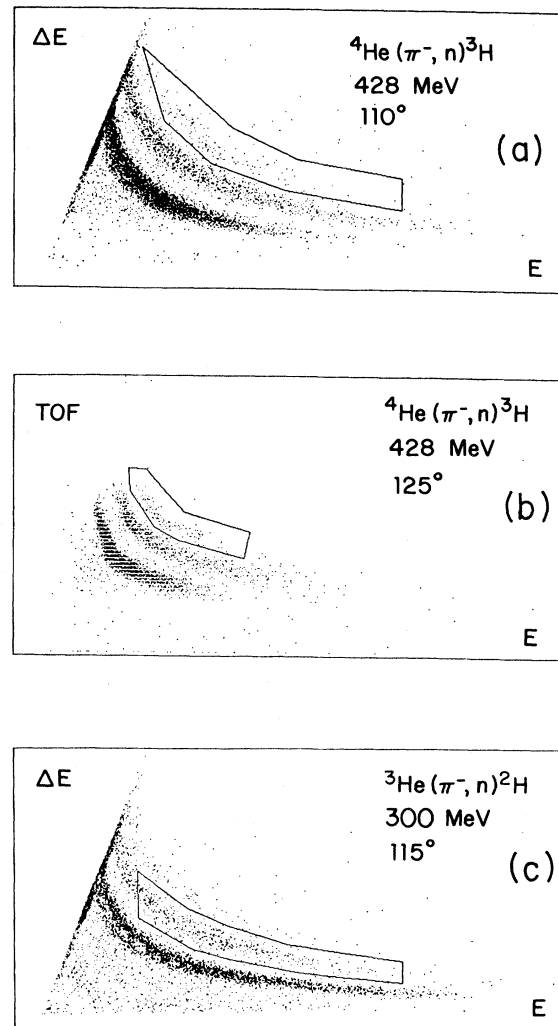

FIG. 7. Typical mass identifications by TOF vs E or dE vs E for (a) ^{4}He$(\pi^-,n)^3$H at $T=428$ MeV and $\theta_{3_H}=110°$, (b) ^{4}He$(\pi^-,n)^3$H at $T=428$ MeV and $\theta_{3_H}=125°$, and (c) ^{3}He$(\pi^-,n)^2$H at $T=300$ MeV and $\theta_{2_H}=115°$. The lowest band is H, the next is ^{2}H, and the third is ^{3}H; note the expected $1/E$ dependence. The selected reaction band is boxed. The linear band $\propto E$ of (a) and (c) represents particles that did not pass entirely through the ΔE counters.

Fig. 7 the first mass band is protons, the second is deuterons, the third is tritons. The large scatter of particles below the proton band is pions and other minimum-ionizing particles. The diffuse scatter above the tritons consists of events that do not have combinations of dE/dx, TOF, or E consistent wth any known reaction; they can only be accidentals or products of nuclear reactions with detector materials. Note the linear $\Delta E_3 \propto E$ segment on the left-hand side of Figs. 7(a) and (c). These are particles that stopped in one of $S1$, $S2$, and $S3$; for them $\Delta E = E$.

In each case, the appropriate mass band for the reaction [i.e., tritons for the ^{4}He target and deuterons for the ^{3}He target, in the case of (π^-,n), or tritons for the ^{3}He target in the case of (π^-,π^0)] was isolated by a computer-graphics technique. Such a region is shown by the outlined polygon. The two-body (π^-,n) or (π^-,π^0) reaction peak would be included in this region, but sometimes was not discernable because of the kinematic broadening due to large angular acceptance. These data were then binned by angle. We chose 5° angular bins as being of sufficient resolution for the angular distributions, and at the same time fine enough to suppress any visible effects of kinematic broadening, without being so fine as to preclude having a reasonable number of events in the bin. If the mass band had been initially isolated by ΔE vs E, a second scatter plot was made where the data were further isolated by TOF vs E. Reciprocally, if the band was initially isolated by TOF vs E, then a second constraint from ΔE vs E was imposed. A typical example of this double mass constraint is displayed in Fig. 8 for the case of ^{3}He$(\pi^-,n)d$. For a detector setting $\theta_D = 115°$, three 5° angular bins are shown for TOF vs E. The two-body peak, not visible in the full 25° acceptance of Fig. 7, can now clearly be seen in Fig. 8. As the angle decreases the energy of the deuterons increases. These data show the deuteron peak moving to the right, changing from 88 MeV at 120° to 98 MeV at 109.5°.

After the data were subjected to mass constraints and angular binning, energy histograms were made for each 5° bin. The two-body peak was readily identifiable in these histograms; a typical example is displayed in Fig. 9. These peaks were then integrated to extract the differential cross section.

E. Extraction of cross sections

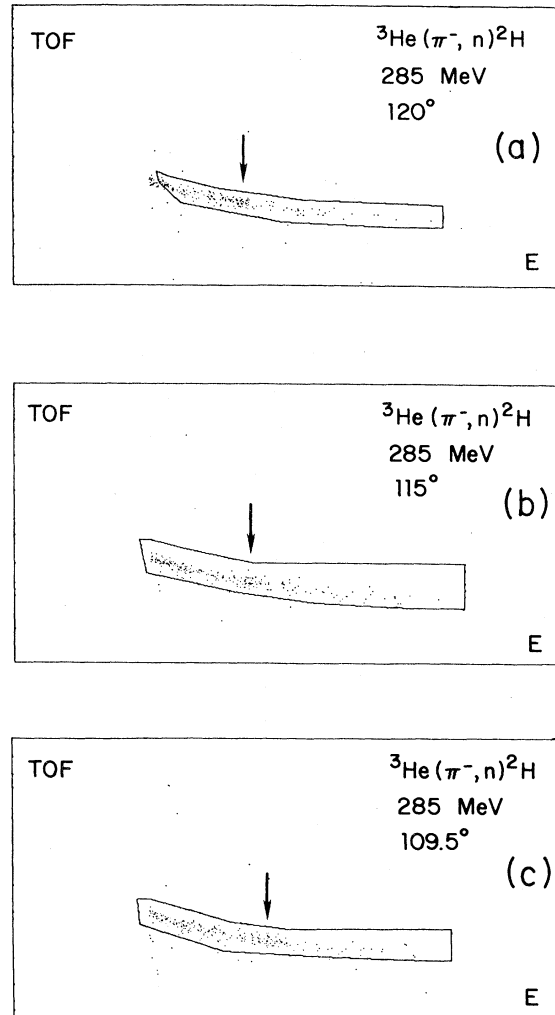The area of each energy peak was divided by the ion chamber counts, which had been adjusted for

FIG. 8. Typical deuteron identification of ^{3}He$(\pi^-,n)^2$H at 300 MeV in 5° bins. These ^{2}H were identified by TOF vs E after the ΔE vs E constraint of Fig. 7(c). The arrow points to a region of higher particle density corresponding to the two-body reaction peak. Note the increase of deuteron energy with angle. (a) $T_{2_H} = 88$ MeV at $\theta_{2_H} = 120°$, and (b) $T_{2_H} = 92$ MeV at $\theta_{2_H} = 115°$, and (c) $T_{2_H} = 98$ MeV at $\theta_{3_H} = 109.5°$.

computer dead time and converted to an absolute cross section by the normalization method discussed in Sec. II A. A correction for detector inefficiency was applied to each spectrum; this was basically the probability that two or more MWPC planes misfired for a "good" event.[2] Then, spectra extracted from different data runs having the same incident pion energy and ^{2}H or ^{3}H recoil angle were summed, to improve the counting statistics. A multiplicative factor accounted for the solid angle ac-
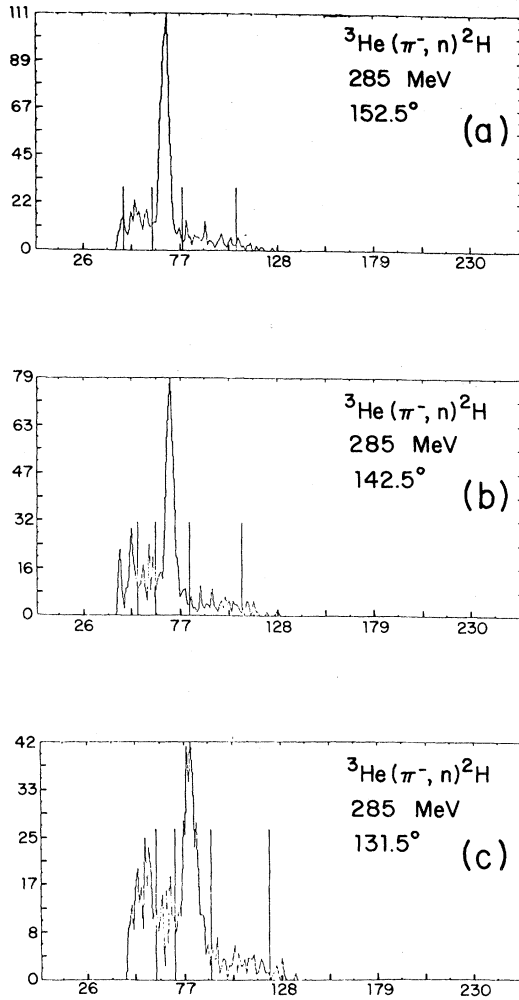
FIG. 9. Raw spectra for ^{3}He$(\pi^-,n)^2$H at $T_\pi = 285$ MeV, for (a) $\theta_{2_H} = 152.5°$, (b) $\theta_{2_H} = 142.5°$, and (c) $\theta_{2_H} = 131.5°$. In each case the large peak is the ^{2}H recoil from (π^-,n), at kinetic energies of (a) 67.5 MeV, (b) 72 MeV, and (c) 78 MeV. Note the peak changes position with increasing energy. The background is deuterons that have been knocked into the continuum by other processes. The four vertical bars represent cuts that define background and peak regions for computation of the cross sections. The abscissa represents channel number, and the ordinate represents particle number.

ceptance (71.4 msr) and the target density (^{3}He, ^{4}He superfluid, and ^{4}He normal fluid, appropriately corrected for target temperature).

The spectrum was a two-body peak superimposed on a structureless background that decreased with increasing recoil energy (cf. Fig. 9). The background under the peak was determined by averaging the background/channel on either side of the peak, and multiplying by the width of the peak. This was

then subtracted from the two-body peak, and the peak was integrated to yield $d\sigma/d\Omega$. (This method of background subtraction gave results consistent with the more tedious subtraction of empty target runs.)

Transformations from the laboratory frame to the center-of-mass were effected with a Jacobian transformation

$$J = \frac{d\Omega_{\text{lab}}}{d\Omega_{\text{c.m.}}} ,$$

hence,

$$\frac{d\sigma}{d\Omega_{\text{c.m.}}} = \frac{d\sigma}{d\Omega_{\text{lab}}} \times J .$$

J is given by

$$\frac{\gamma \cdot p^2(p + \beta \cdot E \cos\theta)}{[(p \sin\theta)^2 + (\gamma(\beta \cdot E + p \cos\theta))^2]^{3/2}} ,$$

where

$$\beta = \frac{\text{pion momentum}}{\text{total lab energy}}$$

$$= \frac{p_\pi}{E_\pi + M_{\text{target}}} ,$$

$$\gamma = (1 - \beta^2)^{-1/2} ,$$

and p, E, and θ refer to the particles's momentum, total energy, and scattering angle, respectively, in the c.m. frame.

A correction was made for particles lost to nuclear reactions in the scintillators. The number of particles lost as a function of range, x, is

$$L(x) \propto e^{-\bar{\sigma}_{\text{tot}} x} ,$$

where

$$\bar{\sigma} = \int_0^{E(x)} dE\, f(E)\sigma(E) ,$$

where f is a weight factor. $L(x)$ has been calculated for protons,[17] and agrees well with measurements.[18] Such information is not available for deuterons and tritons. For these particles we assumed $L(x)$ to be of the same functional form for protons, deuterons, and tritons, except for differences in the total reaction cross sections and scaling of range by the mass. For deuterons we used the approximation $\sigma_d \cong 2\sigma_p$. For tritons, we made use of an existing data point at 220 MeV (Ref. 19) and set

$$L^t(x(E)) = \frac{L^t(x(220 \text{ MeV}))}{L^p(x(220 \text{ MeV}))} L^p(x(E)) .$$

Table VIII summarizes the corresponding correction (multiplicative factors ϕ_d and ϕ_t) for deuterons

TABLE VIII. Correction factors for particles lost to nuclear reactions with scintillator material.

E_d (MeV)	ϕ_d	E_t (MeV)	ϕ_t
30	1	30	1
40	1.01	40	1.005
50	1.02	50	1.01
75	1.05	75	1.04
100	1.09	100	1.075
125	1.15	125	1.12
150	1.23	150	1.205
175	1.34	175	1.31
200	1.48	200	1.47
		225	1.69
		250	2.05

and tritons. ϕ was interpolated to obtain factors for intermediate energies.

The errors introduced by our $d\sigma/d\Omega$ extraction procedure were both statistical and systematic. The total statistical error was a compound of peak and background errors, viz.,

$$\Delta = (\Delta_{peak}^2 + \Delta_{background}^2)^{1/2} ,$$

$$\Delta_{peak} = \left[\sum_i n_i \right]^{1/2} ,$$

where the summed peak counts $\sum_i n_i$ have already been corrected for dead time and MWPC efficiency losses.

$$\Delta_{background} = (B_1 + B_2)^{1/2} \frac{C}{C_1 + C_2} ,$$

where B_1 and B_2 are background counts in the regions on either side of the peak, of channel width C_1 and C_2, respectively. C is the channel width of the peak, and

$$\frac{C}{C_1 + C_2}$$

represents the fraction of the background error $(B_1 + B_2)^{1/2}$ that contributes to the cross-section er-

ror. The determination of average background per channel from the regions adjacent to the reaction peak was consistent with the observed spectrum from an empty target cell, and had the advantage of eliminating systematic differences between data runs. The sources of systematic error are summarized in Table IX; summing these errors in quadrature gives a total systematic error of 16.9%. For the case of SCE data, we adopted a worst-case systematic error of 25% for the background subtraction procedure, which arose mainly from the poor signal-to-noise ratio. Thus, we quote[4] a total systematic error of 30% in the SCE results.

Finally, multiple data points and points with poor statistics were averaged, with a weight factor that was number dependent: If σ_1 and σ_2 are differential cross sections with errors Δ_1 and Δ_2, then:

$$\bar{\sigma} = \frac{a\sigma_1 + b\sigma_2}{a + b} ,$$

where

$$a = \frac{\Delta_1^2 + \Delta_2^2}{\Delta_1^2}$$

and

$$b = \frac{\Delta_1^2 + \Delta_2^2}{\Delta_2^2}$$

are the weight factors that depend on the number of particles that contribute to the cross section. Hence, cross sections with higher error (fewer particle counts) contribute less to the average cross section than those with lower error.

The (π^-, n) differential cross sections were integrated numerically to obtain forward $(\theta \leq 90°)$ cross sections:

$$\sigma(\theta \leq 90°) = 2\pi \int_0^1 \frac{d\sigma}{d\Omega} d(\cos\theta)$$

$$= 2\pi \sum_{\cos\theta=0}^{\cos\theta=1} \left\langle \frac{d\sigma}{d\Omega} \right\rangle_i (0.1) ,$$

TABLE IX. Summary of systematic error.

Source of systematic error	Percentage of error
(π, N) normalizations to experiments of Ref. 5 (the error here is their total systematic error)	$< 15\%$
corrections for nuclear reactions in the scintillators (Refs. 17 and 18)	$< 5\%$
beam contamination (Ref. 9)	1%
error in solid angle from finite beam-spot size (2.5 cm vertical $\times$ 1.5 cm horizontal)	6%

where $\cos\theta$ was incremented in steps of 0.1 and

$$\left\langle \frac{d\sigma}{d\Omega} \right\rangle_i$$

is the average value of $d\sigma/d\Omega$ in the ith interval. An extrapolation to $\cos\theta=0$ was necessary. Forward cross sections for (π^-,π^0) were not computed, because of the limited angular range of the data.

III. RESULTS AND DISCUSSION

The two reactions measured, ^{3,4}He$(\pi^-,n)^{2,3}$H and ^{3}He$(\pi^-,\pi^0)^3$H, are not related to each other in any simple way; hence, we shall discuss them separately.

A. ^{4}He$(\pi^-,n)^3$H and ^{3}He$(\pi^-,n)^2$H

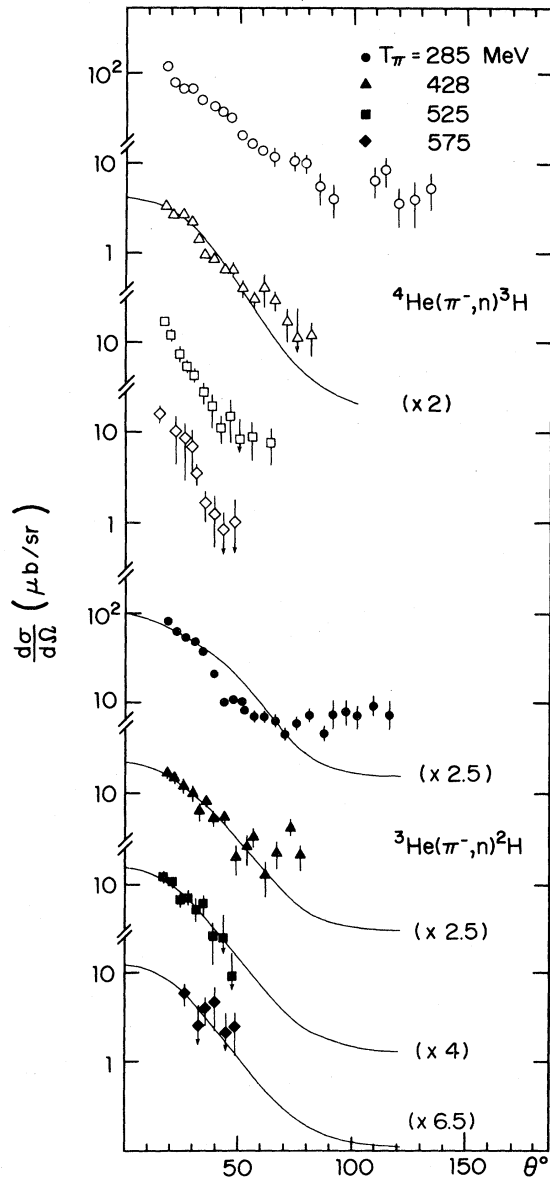The differential cross sections are presented in Figs. 10 and 11 and in Tables X$-$XV. Figure 10

FIG. 10. ^{3,4}He$(\pi^-,n)^{2,3}$H differential cross sections in the c.m. θ is the neutron scattering angle. The solid curve is from Ref. 20.

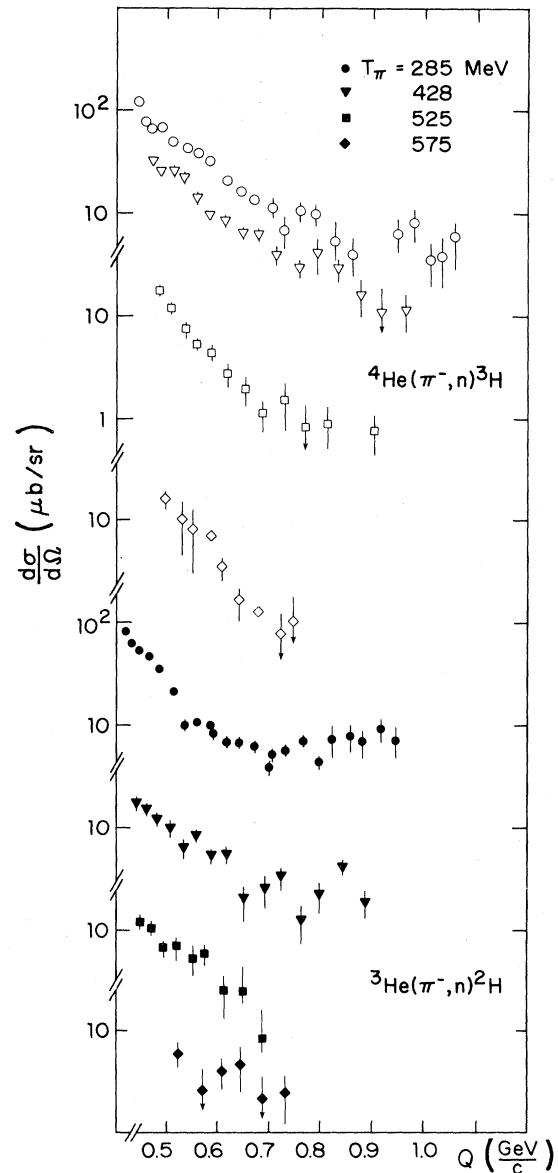
FIG. 11. ^{3,4}He$(\pi^-,n)^{2,3}$H differential cross section in the c.m. vs momentum transfer $|\vec{p}_n - \vec{p}_\pi|$.

TABLE X. c.m. differential cross sections $^4\text{He}(\pi^-,n)^3\text{H}$.

T_π^{lab} (MeV)	θ (deg)	q (MeV/c)	$\dfrac{d\sigma}{d\Omega}$ (μb/sr)
285	18	446	121.5±7.5
	21	457	78.5±5.9
	25	473	67.7±5.6
	29	492	68.4±5.3
	33	512	49.9±4.5
	38	539	43.5±2.0
	42	562	38.2±2.0
	46	586	32.3±1.7
	51	616	20.9±1.7
	56	644	16.8±1.1
	60	672	14.0±1.2
	65	704	11.9±2.5
	69	729	7.1±2.5
	74	760	10.7±2.3
	79	791	10.0±2.3
	85	827	5.6±2.1
	91	862	4.2±1.7
	108	952	6.7±2.4
	114	980	8.6±3.0
	120	1007	3.7±1.7
	127	1035	4.1±2.1
	134	1060	5.4±2.4

shows the results from $^{3,4}\text{He}(\pi^-,n)^{2,3}\text{H}$ vs the barycentric scattering angle of the ejected neutron, and Fig. 11 shows the ^3He and ^4He results as functions of the c.m. three-momentum transfer

TABLE XI. $^4\text{He}(\pi^-,n)^3\text{He}$.

T_π^{lab} (MeV)	θ (deg)	q (MeV/c)	$\dfrac{d\sigma}{d\Omega}$ (μb/sr)
428	18	475	32.5±1.3
	21	491	25.8±1.1
	25	515	26.2±1.1
	28	534	22.3±0.8
	32	562	14.5±0.7
	35	584	9.6±1.0
	39	615	8.6±0.8
	44	651	6.6±0.7
	47	679	6.4±0.9
	52	716	4.0±0.8
	57	758	3.0±0.6
	61	796	4.2±1.7
	66	834	2.9±0.7
	71	879	1.7±0.7
	76	920	1.1±0.8
	82	968	1.2±0.5

TABLE XII. $^4\text{He}(\pi^-,n)^3\text{He}$.

T_π^{lab} (MeV)	θ (deg)	q (MeV/c)	$\dfrac{d\sigma}{d\Omega}$ (μb/sr)
525	17	485	17.6±1.8
	20	504	11.8±1.4
	24	532	7.3±1.4
	27	555	5.2±0.7
	31	583	4.2±0.6
	34	613	2.7±0.7
	38	649	1.9±0.6
	42	682	1.1±0.4
	46	724	1.5±0.8
	50	763	0.8±0.6
	55	807	0.9±0.4
	64	899	0.8±0.3
575	18	496	15.9±3.1
	22	528	10.0±5.6
	25	551	7.8±4.9
	29	586	6.9±3.2
	31	604	3.4±0.9
	35	641	1.6±0.6
	39	680	1.2±0.7
	43	720	0.7±0.6
	48	746	1.0±0.8

$q = |\vec{p}_\pi - \vec{p}_n|$. It is important to note the slow variation of the measured cross sections: The magnitude decreases only a factor of 10 over the angular range $\theta = 20° - 120°$, corresponding to the momentum transfer range $q = 0.4 - 1.1$ GeV/c, suggesting the possibility of a momentum-sharing (i.e., multinucleon) mechanism. The variation with incident energy is also small, decreasing by only a decade or so for ^3He and by two decades for ^4He, over an incident energy range of 300 MeV, from 285 − 575 MeV.

These results may be compared with predictions[20] of Fearing based on a two-nucleon absorption mechanism, diagrammed in Fig. 3(a). In this model the differential cross section is expressed as a product of the fundamental two-nucleon pion absorption vertex, represented by ($\pi d \rightarrow pp$), and a form factor for a correlated two-nucleon pair, a "quasideuteron," in the nucleus. Since the two-nucleon absorption vertex is not readily subject to calculation, the measured cross sections for $\pi d \rightarrow pp$ are used instead. Symbolically,

$$d\sigma(\text{He}(\pi^-,n)) \propto d\sigma(\pi d \rightarrow pp) \times F^2(K) .$$

Here

TABLE XIII. c.m. differential cross-sections ^{3}He$(\pi^-,n)^2$H.

T_π^{lab} (MeV)	θ (deg)	q (MeV/c)	$\dfrac{d\sigma}{d\Omega}$ (μb/sr)
285	19	418	80.6±3.8
	22	432	63.7±3.3
	26	446	53.9±3.1
	30	465	47.2±3.1
	34	486	36.3±2.4
	39	512	20.8±1.4
	43	536	10.2±1.1
	47	560	10.7±1.0
	51	585	10.0±1.1
	52	589	8.3±0.9
	56	613	6.8±1.0
	57	618	7.3±0.9
	61	640	7.0±0.9
	65	669	6.5±0.8
	66	673	6.2±0.9
	70	700	3.9±0.6
	71	705	5.4±0.8
	75	730	5.9±0.8
	81	764	7.4±0.9
	87	797	4.6±0.7
	91	821	7.7±2.6
	97	853	8.3±2.5
	102	882	7.3±2.3
	109	914	9.6±2.4
	116	943	7.5±2.5

$$K \sim \frac{A-2}{A-1}q \; ;$$

K is essentially the momentum transfer to the

TABLE XIV. ^{3}He$(\pi^-,n)^2$H.

T_π^{lab} (MeV)	θ (deg)	q (MeV/c)	$\dfrac{d\sigma}{d\Omega}$ (μb/sr)
428	19	441	17.6±2.1
	22	460	15.3±1.9
	26	480	12.3±1.7
	30	506	10.1±1.9
	33	532	6.5±1.5
	36	554	8.7±1.2
	40	584	5.5±0.9
	44	615	5.6±1.0
	49	652	2.0±0.8
	54	689	2.6±0.9
	57	719	3.3±0.8
	62	758	1.3±0.5
	67	795	2.2±0.8
	73	841	4.4±0.9
	78	883	2.0±0.6

TABLE XV. ^{3}He$(\pi^-,n)^2$H.

T_π^{lab} (MeV)	θ (deg)	q (MeV/c)	$\dfrac{d\sigma}{d\Omega}$ (μb/sr)
525	18	449	12.4±1.6
	21	471	10.6±1.5
	25	493	6.8±1.2
	28	521	7.0±1.5
	32	551	5.4±1.7
	35	577	5.9±1.4
	39	612	2.5±1.2
	44	652	2.4±2.1
	47	685	0.9±0.8
575	27	518	5.9±1.7
	33	571	2.5±1.8
	36	606	3.9±1.3
	40	641	4.7±2.5
	45	685	2.1±1.5
	49	729	2.4±1.2

quasideuteron. $F(K)$ is the Fourier transform to momentum space of the threefold overlap of wave functions of the initial and final nuclei and the quasideuteron. Included in $F(K)$ are factors to account for distortion of the incoming and outgoing waves; thus, the distortions contain the effects of any $\pi + N$ scattering that precedes the pion absorption. The results of these calculations are represented by the solid curves in Fig. 10. This particular model underestimates the data by a factor which is 2.5 at 285 MeV, increasing to a factor of 6.5 at 575 MeV.

In order to examine the energy dependence directly, we consider the forward cross section

$$\sigma_F = \int_1^0 \frac{d\sigma(\cos\theta)}{d\Omega} d(\cos\theta) \; ;$$

the integration over $\cos\theta$ effectively averages the momentum transfer for the angular region $\theta = 0° - 90°$, where θ is the barycentric scattering angle of the ejected neutron. The total cross section would be a more traditional quantity to use here, but our large angle data are too sparse to yield reliable values. The results are displayed in Fig. 12, along with data from a previous experiment.[5] Also shown as a solid curve is the total cross section $\sigma(\pi d \to pp)$.[21] The $\pi d \to pp$ reaction is symmetric in the forward and backward hemispheres, and

$$\sigma_F(\pi d \to pp) = \tfrac{1}{2}\sigma_{tot}(\pi d \to pp) \; ,$$

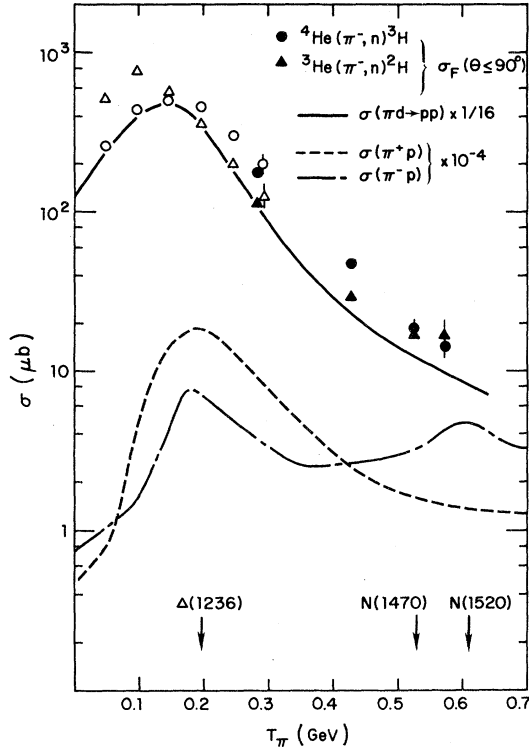so it is meaningful to compare $\sigma_F(\pi + \text{He})$ with $\sigma_{tot}(\pi + d)$.

FIG. 12. The energy dependence of ^{3,4}He$(\pi^-,n)^{2,3}$H. The solid points represent the forward cross sections from ^{4}He, and the solid triangles represent those from ^{3}He. The open points and triangles are from the data of Ref. 5. The solid line is $\frac{1}{16}\times\sigma_{tot}$ $(\pi d \rightarrow pp)$ as in Ref. 21. The dashed and dotted-dashed curves are $10^{-4}\times$ the total pion-nucleon cross sections (Ref. 22) and the arrows indicate the pion kinetic energies at which resonances are excited on the free nucleons.

We see that the energy dependence of the forward cross sections for ^{3,4}He$(\pi^-,n)^{2,3}$H tracks that of ^{2}H(π^+,p)H quite closely. This is remarkable; if pion absorption does indeed proceed according to the mechanism of Fig. 3(a), then the presence of $F_d^2(K)$ should suppress the cross sections at higher energies, since F^2 decreases with increasing momentum transfer. The persistence of the cross sections at high energies suggests the action of mechanisms absent in the elementary $\pi d \rightarrow pp$ reactions.

Part of the slow variation of σ_F with T_π is explained when we note that $F^2(K)$ does not vary as rapidly as one might first expect. The bulk of σ_F is determined by the forward-angle cross sections; for example, in the case of ^{4}He$(\pi^-,n)^3$H 90% of σ_F is from $\theta \leq 46°$ at 285 MeV, and from $\theta \leq 20°$ at 575 MeV. In these instances the range of q is $\sim 0.40-0.60$ GeV/c and $0.44-0.55$ GeV/c, respec-

tively. Thus, the range of ΔK ($\approx \frac{2}{3}\Delta q$) sampled at both these energies is about the same. Consequently, the energy dependence we see is that of the πNN vertex exclusive of any form-factor dependence. This is rather reassuring, considering that one formulates these multinucleon schemes specifically because (π,N) cross sections *do not* exhibit a strong dependence on q.

We see, then, that $\pi d \rightarrow pp$ does indeed account for a substantial part of the ^{3,4}He$(\pi^-,n)^{2,3}$H reaction, and $F^2(K)$ could not substantially affect the energy dependence of these data over the range of incident energies measured here. There is, however, another effect that should contribute to the σ_F at higher energies. In Fig. 12 we show the total cross sections for pion-proton scattering,[22] $\sigma(\pi^+p)$ (dashed curve) and $\sigma(\pi^-,p)$ (dotted-dashed curve). $\sigma(\pi^+p)$ shows the peak at $T_\pi=0.2$ GeV characteristic of the formation of the $I=\frac{3}{2}$ resonance. The formation of this resonance in ^{2}H, as well as in ^{3}He and ^{4}He, accounts for the broad peak in the energy dependence at $T_\pi \sim 0.2$ GeV. The next resonances that can be induced are the $T=\frac{1}{2}N^*(1470)$ and $N^*(1520)$, with free widths of ~ 230 MeV and 125 MeV, respectively. Our pion absorption data are in the energy region where we can indeed excite these resonances in ^{3,4}He, which would have the effect of enhancing the cross sections relative to ^{2}H. These resonances are suppressed in ^{2}H, because there the (pn) pair is in an $I=0$ state, which discriminates again the $I=\frac{1}{2}\pi^-+p$ scattering in $\pi+d\rightarrow n+n$.[23] In ^{3,4}He, however, there are $I=1(NN)$ "quasideuteron" pairs on which the reaction of Fig. 3(a) could proceed, through π^-+p scattering, and excitation of the $I=\frac{1}{2}N^*(1470)$ and $N^*(1520)$ resonances suggests a natural explanation for the enhanced pion-absorption at large T_π. Recent theoretical work[24] by Yoo and Landau addresses the question of pion absorption on pp/nn pairs, with particular attention to the effect of these ρ^2 terms on the pion-nuclear optical potential. This calculation is an extension of Mandelstam's isobar model,[25] which includes the effect of the intermediate Δ. However, it is necessary that explicit calculations be done for ^{3,4}He$(\pi^-,n)^{2,3}$H incorporating the effect of the isospin-$\frac{1}{2}$ resonances to verify the suppositions presented here regarding their effects on the energy dependence of the cross sections.

B. ^{3}He$(\pi^-,\pi^0)^3$H

In Fig. 13 and Table XVI we present the center-of-momentum frame differential cross sections vs

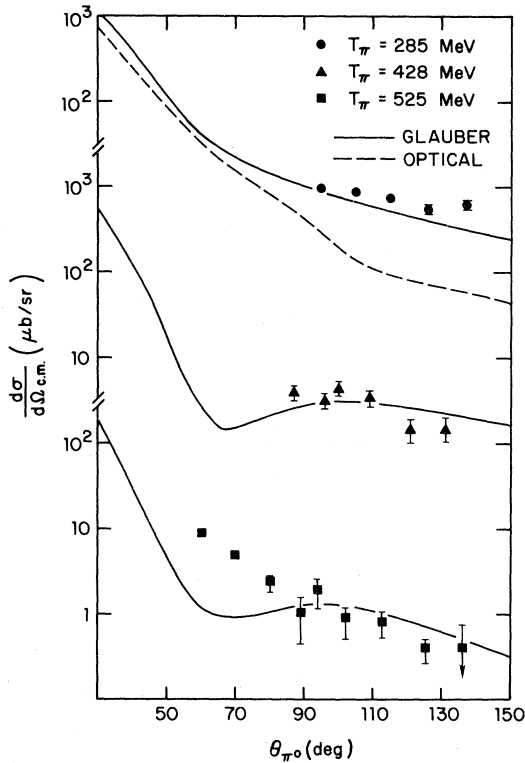FIG. 13. The differential cross sections from ^{3}He$(\pi^-,\pi^0)^3$H in the c.m. vs scattering angle of the π^0. The solid curve is the Glauber model calculation of Ref. 26 and the dotted-dashed curve is an optical potential calculation of Ref. 1.

TABLE XVI. c.m. differential cross sections ^{3}He$(\pi^-,\pi^0)^3$H.

T_π^{lab} (MeV)	θ (deg)	q (MeV/c)	$\dfrac{d\sigma}{d\Omega}$ (μb/sr)
285	95	516	9.8$\pm$0.8
	105	557	9.0$\pm$0.7
	115	592	6.6$\pm$0.6
	126	626	5.6$\pm$0.6
	137	653	6.3$\pm$0.6
428	89	651	4.0$\pm$0.8
	96	691	3.3$\pm$0.6
	100	709	4.5$\pm$0.8
	109	757	3.5$\pm$0.7
	121	806	1.5$\pm$0.5
	131	846	1.5$\pm$0.5
525	60	560	9.0$\pm$1.0
	70	611	4.9$\pm$0.6
	80	688	2.3$\pm$0.5
	89	750	1.1$\pm$0.6
	94	782	1.9$\pm$0.5
	102	833	0.9$\pm$0.4
	113	890	0.8$\pm$0.3
	125	951	0.4$\pm$0.1
	136	993	0.4$\pm$0.36

π^0 scattering angle. Salient features of the data are the following: (1) the weak dependence of the cross sections with respect to scattering angle; the data vary by a factor of 20 at most (for $T_\pi = 525$ MeV), over an angular range from $60°-140°$ (which corresponds to a momentum transfer range $q = 0.5 - 1.0$ GeV/c, with $q = |\,\vec{p}_{\pi^-} - \vec{p}_{\pi^0}\,|$; (2) the weak variation with incident energy, by only a factor of 10 over a range from $T_\pi = 290 - 525$ MeV. Also shown are traditional attempts to describe single-charge exchange (SCE): a Glauber model calculation by Gerace and collaborators[26] (solid curve), and an optical potential calculation by Landau[1] (dotted-dashed curve; 290 MeV only, the highest energy for which such a calculation exists).

The Glauber calculation includes s- and p-wave phase shifts for the πN amplitude $t_{\pi N}$, uses "realistic" ^{3}He form factors[7] as input, and retains terms linear in $\vec{\sigma}\cdot\vec{n}$, the spin-flip term of the Hamiltonian (which is directly related to magnetic scattering). It is found that most of the cross section is due to single scattering, and that spin flip dominates SCE for

$\theta = 60° - 120°$ and $T_\pi > 150$ MeV. This prediction of the data is surprisingly good, considering (1) a Glauber model is only supposed to describe forward scattering, and (2) the valid kinematic region is that of $kr \gg 1$, where $k =$ incident pion momentum and $r =$ nuclear radius. However, the Glauber model involves an integral overall pion momenta; the πN amplitude $t_{\pi N}$ is experimentally determined for physical momentum transfers $q \leq 2k$, and $t_{\pi N}$ in the unphysical region $q > 2k$ must be obtained by parametrization.

The ^{3}He magnetic form factor used in this calculation was obtained from a fit to electron scattering data up to $q \approx 700$ MeV/c, and has a minimum extrapolated to occur at $q \approx 780$ MeV/c, with a decrease by ~ 3 orders of magnitude over the momentum range of interest (i.e., from $600-780$ MeV/c). In Fig. 14 we display our SCE data as a function of $q = |\,\vec{p}_{\pi^-} - \vec{p}_{\pi^0}\,|$. We also show the ^{3}He magnetic form factor, $F_m(q)$, of McCarthy et al.[7] and the new measurements of Cavedon et al.,[8] extending out to $q \approx 1000$ MeV/c in which the minimum is observed at $q = 900$ MeV/c. In the range from $600-900$ MeV/c the magnetic form factor decreases by 5 orders of magnitude. In this same
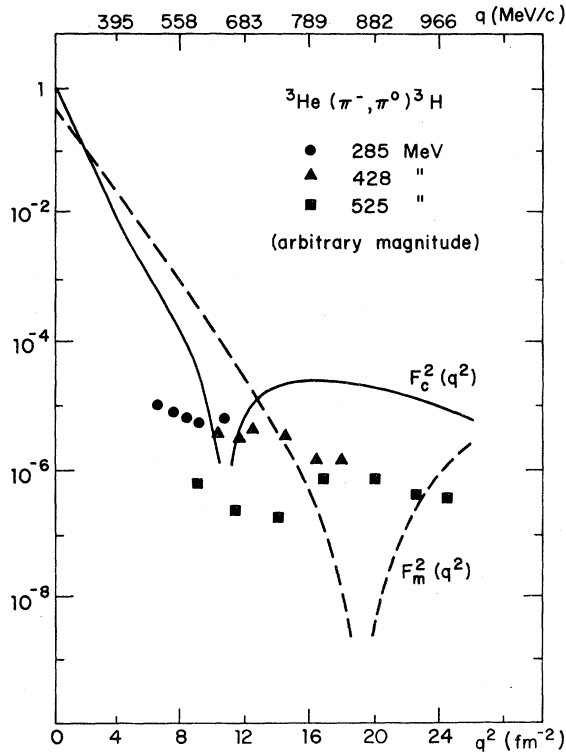
FIG. 14. Our SCE cross sections (in arbitrary units) vs q^2 are denoted for various incident energies. Also shown are the ^{3}He charge form factor of Ref. 7 (solid curve), and the form factor of Refs. 7 and 8 (dashed curve). The electron data are given vs q_{lab}, but $q_{lab} = q_{c.m.}$ to $<15\%$.

range our SCE data fall off by only a factor of 10, i.e., they do not exhibit the strong variation with q that one would expect from the spin-flip dominance in a single-scattering model.

We suggest that this discrepancy can be accounted for by a reassessment of the relative strengths of the spin-flip and non-spin-flip amplitudes. Note that the charge form factor, also plotted in Fig. 14, goes through a minimum at ~ 670 MeV/c, followed by a maximum at ~ 800 MeV/c, rising through 2

orders of magnitude in the very region where F_m^2 goes plummeting downwards. The ^{3}He charge form factor, $F_c^2(q)$, which enters through the non-spin-flip amplitude, may exhibit a sufficiently strong effect to compensate for the magnetic scattering, yielding isotropy with respect to q. This in turn would explain the weak dependence with scattering angle and incident energy cited earlier, and leads to the conclusion, not previously anticipated, that $\pi^- + {}^3$He scattering is not a sensitive probe of the ^{3}He magnetic form factor.[1]

For single scattering, the Glauber model is equivalent to the first order optical model. First order optical model calculations have been computed[1,27] for the ^{3}He$(\pi^-,\pi^0)^3$H up to 295 MeV. Essential features are the following: (1) a first order momentum space potential in a relativistic wave equation; (2) a πN amplitude $t_{\pi N}$ determined from πN phase shifts, including finite size effects; and (3) "realistic" form factors. At 295 MeV the optical model predictions are lower than the Glauber result and underestimate the data by a factor of 10. Second order effects were found to be small, $\lesssim 25\%$. The low cross section of the optical model is most likely attributable to effects of the nuclear medium, since $t_{\pi N}$ comes from free-nucleon scattering.

A valuable feature of SCE is that one can directly examine the isospin-rotation invariance of the pion-nuclear Hamiltonian. This can be done by appealing to the well-known triangle inequality. Briefly, the π-nuclear amplitude $T_{\pi A}$ is assumed to be isoscalar in character; hence

$$T_{\pi A} = T_s + T_v \vec{\mathrm{I}}_\pi \cdot \vec{\tau}_A$$

where T_s and T_v are the isoscalar isovector amplitudes, respectively, and $\vec{\mathrm{I}}_\pi, \vec{\tau}_A$ are the isotopic spinors for the pion and target nucleus, respectively. For an isospin-$\frac{1}{2}$ nucleus it follows[28] that

$$[(d\sigma_{\pi^+})^{1/2} + (d\sigma_{\pi^-})^{1/2}]^2 \geq 2d\sigma_{SCE} \geq [(d\sigma_{\pi^+})^{1/2} - (d\sigma_{\pi^-})^{1/2}]^2 \, ,$$

where $d\sigma_{\pi^+}$, $d\sigma_{\pi^-}$, and $d\sigma_{SCE}$ are the differential cross sections for π^+ elastic scattering, π^- elastic scattering,[29] and SCE scattering, respectively. Figure 15 illustrates the compliance of observations with this inequality at 285 MeV; we see that it is indeed satisfied.

It should be noted that there are discrepancies among the results of the various experiments that have measured pion single charge exchange. Coop-

er and collaborators report the results of measurements[30] from ^{3}He$(\pi^-,\pi^0)^3$H at 200 MeV where the reaction was identified by detection of the two photons from the decay $\pi^0 \rightarrow 2\gamma$. If one extrapolates their angular distribution, measured in the range $\theta = 0° - 90°$, to backward angles $\theta = 100° - 130°$, it appears that the predicted cross sections are $\sim 3 \times$ larger than those reported in Ref. 6 using the triton recoil method similar to that described here
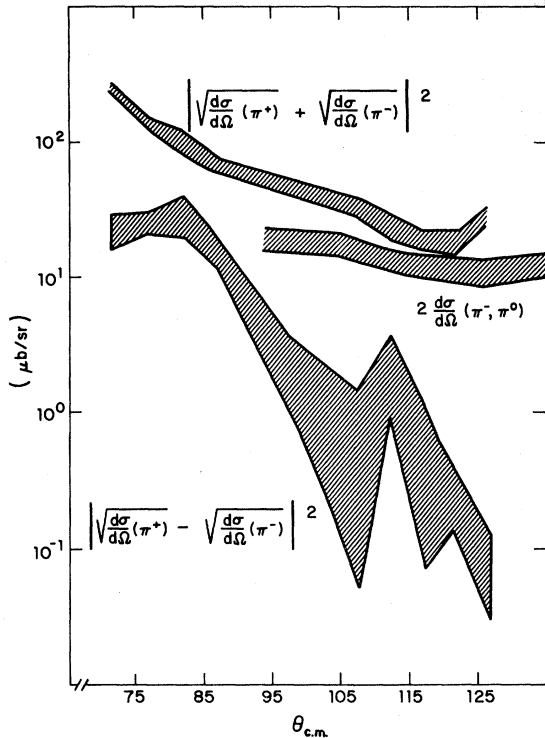
FIG. 15. A test of the triangle inequality for ^{3}He(π^-,π^0)^{3}H at $T_\pi=295$ Mev. The upper band represents the sum of π^+-^{3}He and π^--^{3}He elastic amplitudes, squared. The lower band represents the difference, and the central band is $2\times$SCE. The bands include quoted statistical and systematic errors. The elastic data are from Ref. 29.

(cf. Fig. 3 of Ref. 30). Furthermore, the cross sections of Ref. 6 at 290 MeV are about $1.5\times$larger than our 285 MeV cross sections in the same angular range. So, no two of the three data sets appear to be in agreement. It is necessary that ^{3}He(π^-,π^0)^{3}H be measured at $T_\pi=300$ MeV over a full angular range, in order to verify the overall normalization of all these data sets. Such an experiment has been proposed[31] for the low energy photon (LEP) channel of LAMPF.

IV. SUMMARY AND CONCLUSIONS

We have measured the reactions ^{3,4}He(π^-,n)^{2,3}H for pion incident energies $T_\pi=285$, 428, 525, and

575 MeV. This region is beyond that of the pion-induced $\Delta(1236)$, and approaches that of the $N^*(1470)$ and $N^*(1520)$. The pion absorption data were seen to exhibit an energy dependence in the forward cross sections similar in functional form and rate of descent to that of $\sigma_{\text{total}}(\pi d\to pp)$. It is likely that the reaction model is as pictured in Fig. 3(a), and

$$\frac{d\sigma}{d\Omega}(\pi A)\propto\frac{d\sigma}{d\Omega}(\pi d\to pp)\times F^2(K)\ ,$$

where $d\sigma(\pi d\to pp)$ is the fundamental two-nucleon absorption vertex and $F^2(K)$ is the form factor for a two-nucleon pair in the nucleus. The energy dependence of σ_F exhibits some persistence that compensates the expected decrease of F with momentum transfer. It is possible that the presence of $I=1$ pn pairs in He allows the formation of the $I=\frac{1}{2}N^*$ resonances through the process of π^-+p scattering in the two-nucleon vertex, which is discriminated against in the purely $I=0$ state of free deuterium.

We have also measured the reaction ^{3}He(π^-,π^0)^{3}H up to momentum transfers $q=950$ MeV/c, beyond the region of the recently measured[8] minimum in the ^{3}He magnetic form factor. A recent Glauber model calculation[24] has predicted these data quite well, but cannot account for the slow variation with q compared to the rapid variation of F_{mag} of ^{3}He. It seems likely that the non-spin-flip, charge-dependent scattering is of sufficient strength to compensate for the rapid decrease of F_{mag}, since F_c has a maximum where F_{mag} has a minimum.

We have further assessed the presumed isospin-rotation invariance of the π-^{3}He Hamiltonian, by examination of the triangle inequality. This relation, which assumes an isoscalar Hamiltonian and isospin-$\frac{1}{2}$ target, relates the elastic and charge exchange amplitudes, was found to be valid to our level of sensitivity in this high-energy region.

[1]Rubin H. Landau, Phys. Rev. C 15, 2127 (1977).
[2]L. Orphanos, Ph.D. thesis, University of Viginia, 1980.
[3]L. Orphanos, J. Källne, R. Altemus, P. C. Gugelot, J. S. McCarthy, R. C. Minehart, P. A. M. Gram, B. Höistad, C. L. Morris, E. A. Wadlinger, and C. Perdrisat, Phys. Rev. Lett. 46, 1562 (1981).

[4]J. Källne, R. Altemus, P. C. Gugelot, J. S. McCarthy, R. C. Minehart, L. Orphanos, P. A. M. Gram, B. Höistad, C. L. Morris, E. A. Wadlinger, and C. F. Perdrisat, Phys. Rev. C 25, 1098 (1982).

[5]J. Källne, J. E. Bolger, M. J. Devereaux, and S. L. Verbeck, Phys. Rev. C 24, 1102 (1981), and references therein.

[6]J. Källne, H. A. Thiessen, C. L. Morris, S. L. Verbeck, M. J. Devereaux, G. R. Burleson, J. S. McCarthy, R. R. Whitney, J. E. Bolger, C. F. Moore, and C. A. Goulding, Phys. Rev. Lett. 42, 159 (1979).

[7]J. S. McCarthy, I. Sick, and R. R. Whitney, Phys. Rev. C 15, 1396 (1977).

[8]J. M. Cavedon, L. S. Cardman, B. Frois, D. Goutte, M. Huet, Ph. Leconte, J. Martino, X. H. Phan, S. K. Platchkov, S. E. Williamson, W. Boeglin, I. Sick, and P. deWitt Huberts, Proceedings of the Ninth International Conference on High Energy Physics and Nuclear Structure, Versailles, France, 1981.

[9]Richard D. Verbeck and Robert J. Macek, IEEE Trans. Nucl. Sci. NS-22, 1598 (1975).

[10]George J. Krausse and Peter A. M. Gram, Nucl. Instrum. Methods 156, 365 (1978).

[11]E. A. Wadlinger, LAMPF Report LA-6273-MS, 1976.

[12]P. J. Bussey, J. R. Carter, D. R. Dance, D. V. Bugg, A. A. Carter, and A. M. Smith, Nucl. Phys. B58, 363 (1973).

[13]P. M. Ogden, D. E. Hagge, J. A. Helland, M. Banner, J.-F. Detoeuf, and J. Teiger, Phys. Rev. 137, B1115 (1965).

[14]J. D. Jackson, *Classical Electrodynamics* (Wiley, New York, 1962), p. 629.

[15]J. P. Egger, IEEE Trans. Nucl. Sci. NS-20, 1 (1973). L. Costrell, AEC NIM Committee Report TID-20893 (1974).

[16]J. B. Birks, Proc. Phys. Soc. (London) A64, 874 (1951).

[17]D. F. Measday and C. Richard-Serre, Nucl. Instrum. Methods 76, 45 (1969).

[18]A. M. Sourkes, M. S. deJong, C. A. Goulding, W. T. H. van Oers, E. A. Ginkel, R. F. Carlson, A. J. Cox, and D. J. Margaziotis, Nucl. Instrum. Methods 143, 589 (1977); J. M. Cameron, P. Kitching, R. H. McCamis, C. A. Miller, G. A. Moss, J. G. Rogers, G. Roy, A. W. Stetz, C. A. Goulding, and W. T. H. van Oers, *ibid.*,

399 (1977).

[19]N. Willis, I. Brissaud, L. Bimbot, Y. Le Bornec, and B. Tatischeff, Nucl. Phys. A233, 121 (1974).

[20]H. W. Fearing, Phys. Rev. C 16, 313 (1977); J. H. Alexander and H. W. Fearing, in *Meson-Nuclear Physics— 1976* (Carnegie-Mellon Conference), Proceedings of the International Topical Conference on Meson-Nuclear Physics, AIP Conf. Proc. No. 33, edited by P. D. Barnes, R. A. E. Eisenstein, and L. S. Kisslinger (AIP, New York, 1976), p. 468.

[21]D. F. Measday and G. A. Miller, Annu. Rev. Nucl. Part. Sci. 29, 121 (1979); C. Richard-Serre, W. Hirt, D. F. Measday, E. G. Michaelis, M. J. M. Saltmarsh, and P. Skarek, Nucl. Phys. B20, 413 (1970); H. L. Anderson, M. S. Dixit, H. J. Evans, K. A. Klare, D. A. Larson, M. V. Sherbrook, R. L. Martin, D. Kessler, D. E. Nagle, H. A. Thiessen, C. K. Hargrove, E. P. Hincks, and S. Fukui, Phys. Rev. D 3, 1536 (1971).

[22]*Structure of the Nucleus,* M. A. Preston and R. K. Bhaduri (Addison-Wesley, New York, 1975), p. 12.

[23]J. Chahoud, A. Russo, and F. Selleri, Phys. Rev. Lett. 11, 506 (1963).

[24]K.-B. Yoo and R. H. Landau, Phys. Rev. C 25, 489 (1982).

[25]S. Mandelstam, Proc. R. Soc. (London) A244, 491 (1958).

[26]W. J. Gerace, J. P. Mestre, J. F. Walker, and D. A. Sparrow, Phys. Rev. C 22, 1197 (1980); J. P. Mestre, Ph.D. thesis, University of Massachusetts, 1979.

[27]M. Wakamatsu, Nucl. Phys. A340, 289 (1980).

[28]*Theory of Meson Interactions with Nuclei,* J. M. Eisenberg and D. S. Koltun (Wiley, New York, 1980), p. 246.

[29]J. Källne, J. F. Davis, J. S. McCarthy, R. C. Minehart, R. R. Whitney, R. L. Boudrie, J. McClelland, and A. Stetz, Phys. Rev. Lett. 45, 517 (1980).

[30]M. D. Cooper, H. W. Baer, J. D. Bowman, F. H. Cverna, R. H. Heffner, C. M. Hoffman, N. S. P. King, J. Piffaretti, J. Alster, A. Doron, S. Gilad, M. A. Moinester, P. R. Bevington, and E. Winkleman, Phys. Rev. C 25, 438 (1982).

[31]M. D. Cooper and R. R. Whitney, private communication.